This is an open access article published under an ACS AuthorChoice License, which permits copying and redistribution of the article or any adaptations for non-commercial purposes.

ACS OMEGA

Article

Cite This: ACS Omega 2018, 3, 9956−9965

http://pubs.acs.org/journal/acsodf

Microstructural Effect on the Enhancement of Field Electron Emission Properties of Nanocrystalline Diamond Films by Li-Ion Implantation and Annealing Processes

Kamatchi Jothiramalingam Sankaran,*[,†,‡] Chien-Jui Yeh,[§] Srinivasu Kunuku,[§] Joseph Palathinkal Thomas,[∥] Paulius Pobedinskas,[†,‡] Sien Drijkoningen,[†,‡] Balakrishnan Sundaravel,[⊥] Keh-Chyang Leou,[§] Kam Tong Leung,[∥] Marlies K. Van Bael,[†,‡] Matthias Schreck,[#] I-Nan Lin,*[,¶] and Ken Haenen*[,†,‡]

[†]Institute for Materials Research (IMO), Hasselt University, 3590 Diepenbeek, Belgium

[‡]IMOMEC, IMEC vzw, 3590 Diepenbeek, Belgium

[§]Department of Engineering and System Science, National Tsing Hua University, Hsinchu 30013, Taiwan, Republic of China

[∥]WATLab and Department of Chemistry, University of Waterloo, Waterloo, Ontario N2L3G1, Canada

[⊥]Materials Science Group, Indira Gandhi Centre for Atomic Research, Kalpakkam 603102, India

[#]Institute of Physics, University of Augsburg, 86135 Augsburg, Germany

[¶]Department of Physics, Tamkang University, Tamsui 251, Taiwan, Republic of China

ABSTRACT: The impact of lithium-ion implantation and postannealing processes on improving the electrical conductivity and field electron emission (FEE) characteristics of nitrogen-doped nanocrystalline diamond (nNCD) films was observed to be distinctly different from those of undoped NCD (uNCD) films. A high-dose Li-ion implantation induced the formation of electron trap centers inside the diamond grains and amorphous carbon (a-C) phases in grain boundaries for both types of NCD films. Postannealing at 1000 °C healed the defects, eliminated the electron trap centers, and converted the a-C into nanographitic phases. The abundant nanographitic phases in the grain boundaries of the nNCD films as compared to the uNCD films made an interconnected path for effectual electron transport and consequently enhanced the FEE characteristics of nNCD films.

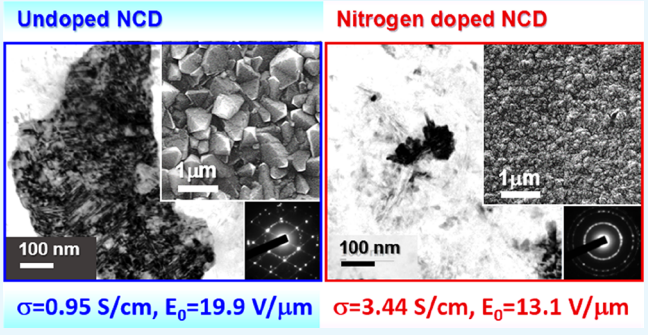

INTRODUCTION

Because of their negative electron affinity and low effective work function, nanocrystalline diamond (NCD) films are systematically investigated for their application as field electron emitters.[1] Though the physical properties of these films rely on the intrinsic structure of the materials, their electrical and optical properties are intimately associated to the microstructure of the films.[2−4] Therefore, the skill to regulate the microstructure and surface morphology of an NCD film could modify this material for a variety of applications such as hard coatings, optical windows, micro-electro-mechanical systems, and electron emitters. An increase of nondiamond carbon phases such as amorphous carbon (a-C) or *trans*-polyacetylene (*t*-PA) is observed when decreasing the diamond grain size.[5] These nondiamond carbon phases (a-C and *t*-PA) act as conducting channels, facilitating easy tunneling of electrons and hence enhance the field electron emission (FEE) properties of NCD films through a "grain boundary conduction emission" mechanism.[6] However, the a-C and *t*-PA phases in the grain boundaries possess a low conductive capacity that limits the FEE properties achievable for NCD films.[7,8] Therefore, for the advancement of NCD-based field emitters, there is a need to control the microstructure; especially, the modification of nondiamond carbon phases is required to improve the electrical conductivity of the materials.

Ion implantation is a possible way to alter the electrical properties of materials through doping with a wide variety of dopant species.[9−11] By proper selection of the implantation energy and dose, the sp^2/sp^3 ratio of diamond and the related carbon materials can be tailored.[10,11] The sp^2-bonded carbon induced during the ion implantation and postannealing treatments of NCD films is the "conductivity promoter", which enables the electrons to move freely inside the films. Lately, numerous reports affirmed that N, O, P, Cu, Au, and Pt

Received: May 24, 2018
Accepted: August 8, 2018
Published: August 27, 2018

Downloaded via UNIV OF WATERLOO on December 31, 2018 at 20:48:50 (UTC).
See https://pubs.acs.org/sharingguidelines for options on how to legitimately share published articles.

ions implanted into diamond can considerably increase the electrical conductivity and FEE properties of diamond materials.[12−16] However, these ions are too large to substitutionally replace C atoms and act as electron donors. Lithium is also an interesting element to be implanted into diamond, as lithium is predicted to be able to occupy the interstitial sites of diamond as a potential shallow donor.[17] Early experiments on Li-ion implantation in diamond films have demonstrated that there is a strong interaction between Li ions and diamond, which leads to the introduction of radiation defects during ion implantation.[18] The diamond films can also exhibit a high electron mobility depending on the energy and dose of Li ions.[19] An enhancement of electrical conductivity and FEE properties for nitrogen-doped NCD films is observed because of Li-ion implantation/annealing processes.[20] Nevertheless, how implanted Li-ions in NCD films effect the microstructure and the electrical properties of these films is not understood yet.

In this paper, a systematic investigation of the effect of Li-ion implantation and annealing processes on the electrical conductivity and FEE behavior of NCD films is reported. We specifically designed NCD films with two different microstructures, that is, undoped NCD (uNCD) and nitrogen-doped NCD (nNCD) films, to investigate how the modification in microstructure impacts the electrical conductivity and FEE properties of the NCD films. A detailed work has been accomplished to disclose the structural and chemical states of these films before implantation, as implanted, and after implantation/annealing processes by using micro-Raman spectroscopy, X-ray photoelectron spectroscopy (XPS), and transmission electron microscopy (TEM). The connection of the microstructure of these films with the improvement of electrical conductivity and FEE characteristics is discussed, emphasizing the role of the microstructure of the starting materials and thereby clarifying the mechanism of Li-ion implantation/annealing processes.

RESULTS

Inset I in Figure 1a shows a scanning electron microscopy (SEM) image of nonimplanted uNCD ($uNCD_{Li0}$), revealing the uniform coverage of the films on Si substrates with a very rough surface. The films contain faceted diamond grains of sizes of around 0.3−0.8 μm with clearly distinguishable grain boundaries. Figure 1a displays a typical bright-field TEM (BF-TEM) micrograph of a $uNCD_{Li0}$ film. The discrete spot patterns in the selective area electron diffraction (SAED, inset II in Figure 1a) are arranged nearly along a ring, implying that the diamond grains are large and randomly oriented. Moreover, the grain boundaries in these films are very sharp with insignificant thickness that is related to the distinctive granular structure of a microcrystalline diamond film.[21] In contrast, inset I in Figure 1b shows an SEM image of a nonimplanted nNCD ($nNCD_{Li0}$) film, indicating nanosized grains of roundish geometry with a very smooth surface. Figure 1b shows a typical BF-TEM micrograph for the $nNCD_{Li0}$ films, whereas inset II in this figure shows the corresponding SAED pattern. There are weak contours delineating the grain boundaries in the BF-TEM micrograph, revealing that these materials comprise diamond grains of a size of about 50−80 nm. Darker contrast regions of the diamond grains are oriented nearly along a zone-axis and diffract electrons intensely, whereas the light contrast regions adjacent to the dark contrast grains are diamond grains that are oriented away from the zone-axis and diffract electrons faintly. The SAED encloses sharp and continuous diffraction rings agreeing with the (111), (220), and (311) lattice planes of the diamond, indicating that the $nNCD_{Li0}$ films are predominantly diamond. A diffuse ring seems to be in the center of the SAED pattern, indicating the presence of sp^2-bonded carbon (nanographitic or a-C phase), along the grain boundaries of the $nNCD_{Li0}$ films.[5]

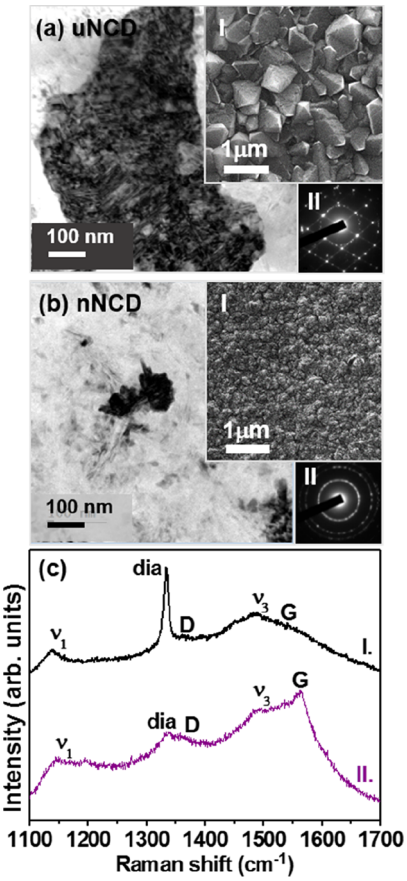

Figure 1. TEM micrographs with corresponding SEM micrographs shown as inset I and the associated SAEDs shown as inset II of (a) uNCD and (b) nNCD films. (c) Micro-Raman spectra of (I) uNCD and (II) nNCD films.

Micro-Raman spectra, displayed in Figure 1c, show that the $uNCD_{Li0}$ films (spectrum I) comprise a sharp diamond resonance peak at 1334 cm^{-1} (indicated as "dia"), which is the typical F_{2g} band for the diamond lattice. Also present are small broad resonance peaks close to 1138 cm^{-1} (ν_1-band) and 1480 cm^{-1} (ν_3-band), corresponding to the distortion modes of CH_x bonds or the *t*-PA phase along the grain boundaries of the $uNCD_{Li0}$ films, and a band at 1540 cm^{-1} (G-band) representing the nanographite phase.[22] In contrast, the diamond peak at ∼1334 cm^{-1} is only barely visible in the Raman spectrum of the $nNCD_{Li0}$ films (spectrum II). These films are dominated by the ν_1-band and ν_3-band resonance peaks, the D-band (1365 cm^{-1}) and G-band (1560 cm^{-1}) resonance peaks, which correspond to sp^2-bonded carbon, that is, disordered carbon and graphite.[23−26] It should be mentioned that the faintness of the diamond peak in spectrum II does not represent that the $nNCD_{Li0}$ films contain no sp^3-bonded carbon. It is attributed to the point that the Raman signal is more responsive to the sp^2-bonded carbon than to the sp^3-bonded carbon when excited with 488 nm.[25]

DOI: 10.1021/acsomega.8b01104
ACS Omega 2018, 3, 9956−9965

The NCD films were then subjected to lithium-ion implantation with an implantation energy of 50 keV. The uNCD films, implanted with Li ions using ion doses of 10^{12} to 10^{14} ions/cm^2, are designated as $uNCD_{Li12}$, $uNCD_{Li13}$, and $uNCD_{Li14}$, respectively. The Li-ion-implanted uNCD films were further annealed at 1000 °C and are designated as $uNCD_{Li12A}$, $uNCD_{Li13A}$, and $uNCD_{Li14A}$. Similarly, the nNCD films are designated as $nNCD_{Li12}$, $nNCD_{Li13}$, and $nNCD_{Li14}$, respectively, when implanted with Li ions using ion doses of 10^{12} to 10^{14} ions/cm^2 and are designated as $nNCD_{Li12A}$, $nNCD_{Li13A}$, and $nNCD_{Li14A}$ postannealing.

The electrical conductivity of both these pristine and Li-ion-implanted NCD films was evaluated using the van der Pauw configuration. Curve I in Figure 2a displays that whereas the

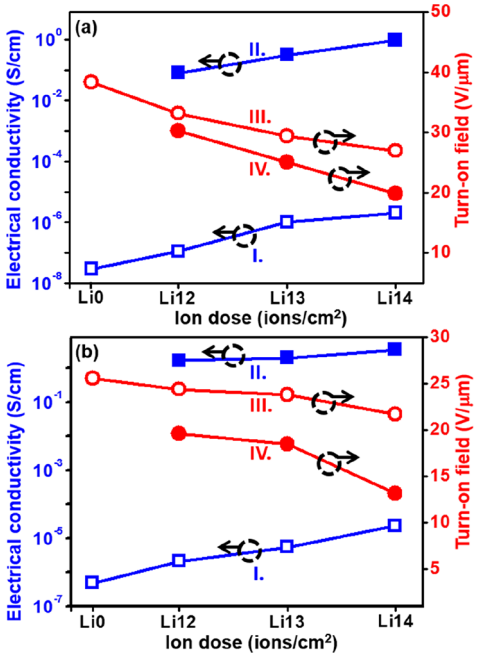

Figure 2. Variation in the electrical conductivity (curves I and II) and turn-on field (curves III and IV) against Li-ion dose before (curves I and III) and after annealing (curves II and IV) for (a) uNCD films and (b) nNCD films.

$uNCD_{Li0}$ films are highly resistive to be assessable using this technique, the electrical conductivity of Li-ion-implanted uNCD films upsurges monotonously with increasing ion dosage, from 1.1 × 10^{-7} S/cm for $uNCD_{Li12}$ films to about 2.0 × 10^{-6} S/cm for $uNCD_{Li14}$ films (curve I, Figure 2a). On annealing, the electrical conductivity value increases abruptly for all Li-ion-implanted uNCD films, reaching a large value of about 0.08, 0.31, and 0.95 S/cm for $uNCD_{Li12A}$, $uNCD_{Li13A}$, and $uNCD_{Li14A}$ films, respectively (curve II, Figure 2a). The nNCD films follow a similar trend as the uNCD films (curves I and II, Figure 2b). The electrical conductivity is low for $nNCD_{Li0}$ films and increases monotonically with the dose of Li-ion implantation. The electrical conductivity value also increased abruptly after annealing, to a large value of 1.64, 1.94, and 3.44 S/cm for $nNCD_{Li12A}$, $nNCD_{Li13A}$, and $nNCD_{Li14A}$ films, respectively. The variations of the conductivity of the uNCD and nNCD films owing to Li-ion implantation and annealing processes are tabulated in Table 1.

Figure 3 depicts the FEE properties of the uNCD and nNCD films implanted with different doses of Li ions, before and after the annealing process. The FEE parameters were extracted from the obtained current density (J)−applied field (E) curves by using the Fowler−Nordheim (F−N) model,[27] the F−N plot, $\ln(J/E^2)$ versus $1/E$, which are shown as insets in Figure 3a. The turn-on field (E_0) nominated here is the lowest value of the F−N plot, representing the intersection of the line segments extrapolated from the low and high electrical field regimes. The variation in E_0 values with different ion implantation doses, before and after annealing, is derived from Figure 3a−d, and is plotted as curves III and IV in Figure 2a,b. For both uNCD and nNCD films, the turn-on field (E_0-value) decreased with an increasing dose of Li-ions (curve III, Figure 2a,b). The annealing process improved markedly the FEE properties, that is, decreased the E_0-value (curve IV, Figure 2a,b). For Li-ion-implanted and annealed uNCD films, the E_0 value decreased monotonously from $(E_0)_{uNCDLi12A}$ = 30.3 V/μm to $(E_0)_{uNCDLi14A}$ = 19.9 V/μm (curve IV, Figure 2a), whereas for the Li-ion-implanted and annealed nNCD films, the E_0 value decreased monotonically from $(E_0)_{nNCDLi12A}$ = 19.6 V/μm to $(E_0)_{nNCDLi14A}$ = 13.1 V/μm (curve IV, Figure 2b). The FEE properties of the materials are also tabulated in Table 1, showing that they are closely correlated with their electrical conductivity. The nNCD series shows markedly higher electrical conductivity and thus enhanced FEE properties than the uNCD series. The $nNCD_{Li14A}$ films show the best electrical conductivity (3.44 S/cm) and FEE behavior (E_0 = 13.1 V/μm) among all the NCD films.

To comprehend how the Li-ion implantation and annealing processes enhance the electrical conductivity and the FEE properties of NCD films, we have accomplished thorough investigations using micro-Raman spectroscopy, XPS, and TEM. Curves I to III in Figure 4a,c display that the Li-ion implantation process insignificantly modifies the Raman spectra of the uNCD and nNCD films, respectively. Curves I to III in Figure 4b,d show that subsequent annealing also does

Table 1. Electrical Conductivity and Turn-On Field Values of Li-Ion-Implanted uNCD and nNCD Films before and after Annealing

		uNCD		nNCD	
	ion dose	electrical conductivity (S/cm)	turn-on field (V/μm)	electrical conductivity (S/cm)	turn-on field (V/μm)
nonimplanted		2.9 × 10^{-8}	38.4	4.9 × 10^{-7}	25.6
as-implanted	10^{12}	1.1 × 10^{-7}	33.2	2.1 × 10^{-6}	24.4
	10^{13}	1.0 × 10^{-6}	29.4	5.5 × 10^{-6}	23.8
	10^{14}	2 × 10^{-6}	27.0	2.3 × 10^{-5}	21.7
after annealing	10^{12}	0.08	30.3	1.64	19.6
	10^{13}	0.31	25.1	1.94	18.5
	10^{14}	0.95	19.9	3.44	13.1

DOI: 10.1021/acsomega.8b01104
ACS Omega 2018, 3, 9956−9965

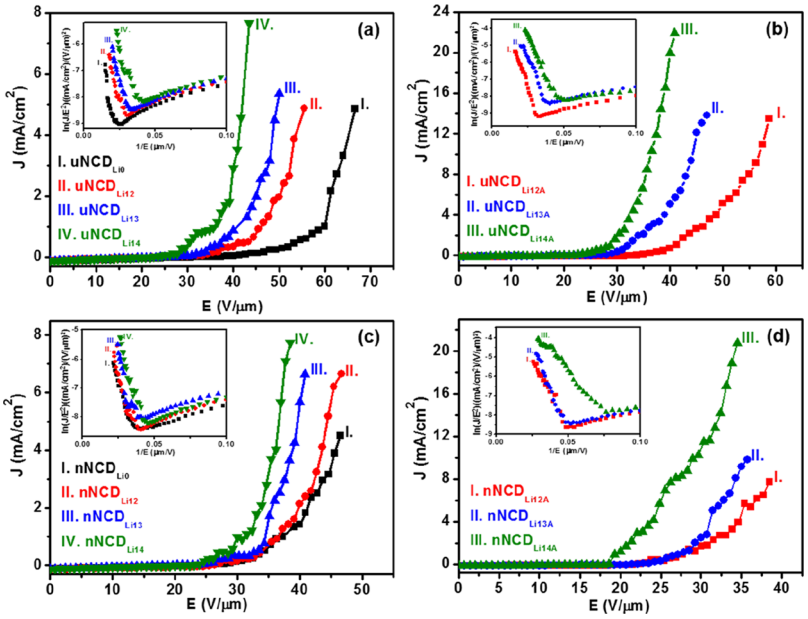

Figure 3. FEE properties (current density-applied field, J–E, curves) measured in a high-vacuum environment for Li-ion-implanted (a,b) uNCD and (c,d) nNCD films, where (a,c) are before and (b,d) are after annealing. The insets show the corresponding F–N plots corresponding to the J–E curves.

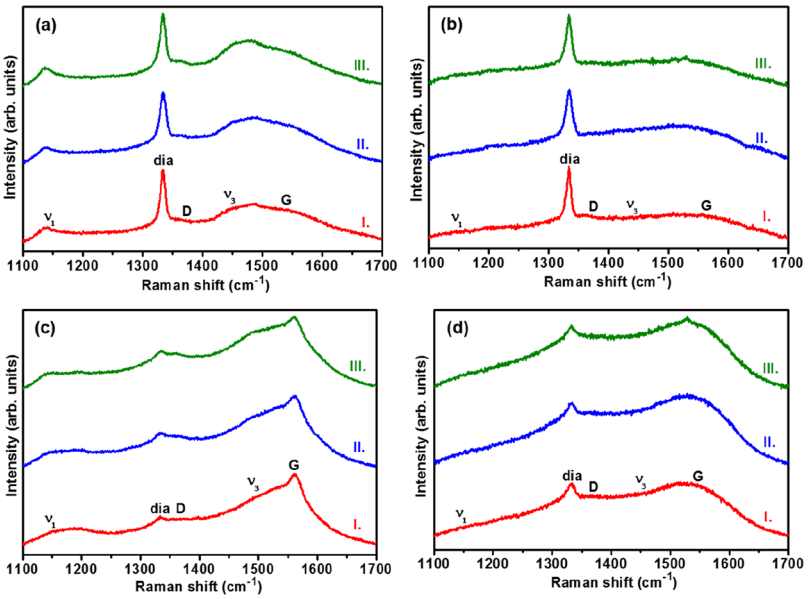

Figure 4. Micro-Raman spectra for Li-ion-implanted (a,b) uNCD and (c,d) nNCD films, where (a,c) are before and (b,d) are after annealing, where the dose of Li ions implanted is (I) 10^{12}, (II) 10^{13}, and (III) 10^{14} ions/cm^2.

not profoundly alter these characteristics. However, detailed analyses reveal some subtle changes because of the Li-ion implantation/annealing processes. It should be mentioned that, in the estimation of the $I_{t\text{-PA}}/(I_D + I_G)$ and the I_D/I_G ratio, the integrated intensities of ν_1, ν_3, D-band, and G-band peaks, that is, $I_{\nu 1}$, $I_{\nu 3}$, I_D, and I_G, were used. These values were taken after normalization of the resonance peaks. Figure 5a shows that, for Li-ion-implanted uNCD films, the $I_{t\text{-PA}}/(I_D + I_G)$ ratio increases (curve I) and the I_D/I_G ratio decreases (curve III) with ion dose. This specifies that ion implantation induces the formation of t-PA and nanographitic phases, which are mainly located in the grain boundaries of uNCD films. Upon annealing, the $I_{t\text{-PA}}/(I_D + I_G)$ and the I_D/I_G ratios show an opposite trend with the ion dose, that is, the $I_{t\text{-PA}}/(I_D + I_G)$ ratio decreases (curve II) and the I_D/I_G ratio increases (curve IV) with ion dose, which indicates the dissociation of CH bonds in the t-PA phase placed at the grain boundaries of the uNCD films, converting them into a highly stable nanographitic phase because of the annealing process.[28] In contrast, Figure 5b shows that the $I_{t\text{-PA}}/(I_D + I_G)$ ratio of nNCD films decreases with ion dose both before (curve I) and after (curve II) annealing. This shows that the net amount of t-PA decreases, comparative to the aggregate of other sp^2-bonded carbon phases in the films, with an increase in ion dose both before and after annealing. The degree of disorder or graphitization of clustered sp^2-bonded carbon phases in the films is evaluated from the I_D/I_G ratio.[29,30] Before and after annealing, the I_D/I_G ratio increases with increasing ion dose

DOI: 10.1021/acsomega.8b01104
ACS Omega 2018, 3, 9956–9965

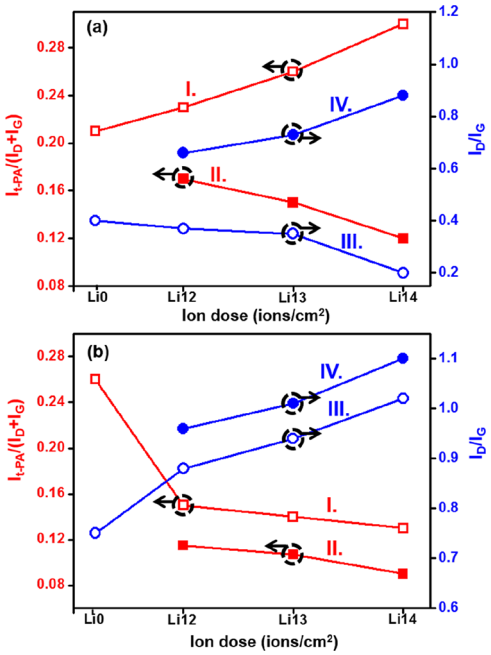

Figure 5. Variation of the $I_{t\text{-PA}}/(I_D + I_G)$ (curves I and II) and I_D/I_G (curves III and IV) with Li-ion dose before and after annealing for (a) uNCD films and (b) nNCD films, where $I_{t\text{-PA}}$, I_D, and I_G are the integrated intensities of the ($\nu_1 + \nu_3$), D-band, and G-band peaks.

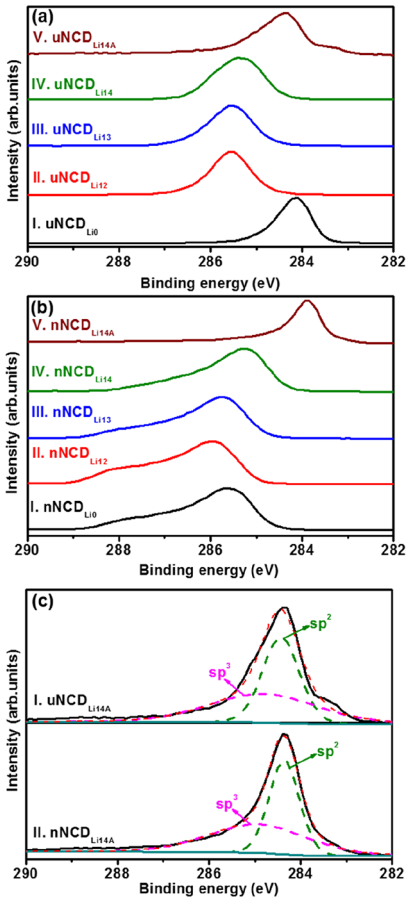

Figure 6. (a,b) C 1s XPS spectra for Li-ion-implanted uNCD (a) and nNCD (b) films before and after annealing where the dose of Li ions implanted is (I) 0, (II) 10^{12}, (III) 10^{13}, and (IV) 10^{14} ions/cm^2 (before annealing) and (V) 10^{14} ions/cm^2 (after annealing). (c) Fitted C 1s XPS spectra for (I) uNCD$_{Li14A}$ and (II) nNCD$_{Li14A}$ films.

(curve III and curve IV) for the nNCD films, indicating the increase in the formation of nanographite from a-C relative to the sp^3 content. The transformation of the phases occurred as said by a three-stage model of increasing disorder in carbon materials.[25,26] Restated, there is a conversion of the grain boundary *t*-PA phase into the nanographitic phase or from diamond (sp^3-bonded carbon) to sp^2 content owing to Li-ion implantation and annealing processes.

It is known that the modification of surface properties can also have a very important impact on the conductivity and FEE properties of the materials.[31,32] To recognize how the Li-ion implantation/postannealing processes possibly modify the surface characteristics of NCD films, XPS studies were accomplished. Carbon 1s (C 1s) core level peaks obtained from XPS spectra for nonannealed and annealed Li-ion-implanted uNCD and nNCD films are shown in Figure 6a,b, correspondingly. The C 1s peak of uNCD$_{Li0}$ (spectrum I, Figure 6a) is observed at 284.1 eV, which is ascribed to bulk diamond.[33] The ion implantation process results in a blue shift for C 1s (spectra II, III, and IV of Figure 6a). The blue shift for the C 1s peak is caused by the presence of surface charges linked to the presence of electron-trapping centers in these films.[34,35] The extent of the blue shift does not seem to change appreciably with the dose of ion implantation. In as-grown films, the H$^-$ ions are absorbed in point defects (vacancies) present in the NCD films, compensating for dangling bonds, and no surface charging phenomenon was observed.[36] Li-ion implantation causes the exclusion of H$^-$ and exposes the dangling bonds, which can then perform as trapping centers for electrons, inducing the observed C 1s blue shift.[37] The increase in the Li-ion dose does not further change this behavior. After annealing, the C 1s peak inversely shifts toward the normal C 1s peak (284.3 eV) for the uNCD$_{Li14A}$ films (spectrum V, Figure 6a), which can be accounted for by the healing of defects. The electrical conductivity of the uNCD$_{Li14A}$ films was thus enhanced.[36] The data not shown here reveal that a similar phenomenon, that is, the reverse shift of the blue-shifted C 1s peak to normal C 1s position because of the annealing process, is also observed for the uNCD$_{Li12A}$ and uNCD$_{Li13A}$ films, which is also accounted for by the healing of the point defects in these materials.

Similarly, Li-ion implantation also induced a marked blue shift of the C 1s peak for the nNCD series of samples (spectra II to IV, Figure 6b), and the blue-shifted C 1s peak was also reversely shifted back to the normal position because of the annealing process (spectrum V, Figure 6b). The elimination of electron trap centers because of the compensation of dangling bonds (or the healing of the atomic defects) during annealing is apparently an important factor, which enhances the electrical conductivity and the FEE properties of the materials. It should be mentioned that the C 1s peak of the nNCD$_{Li0}$ sample (spectrum I of Figure 6b) is observed at 285.6 eV, which is 0.6 eV higher compared to the normal C 1s peak (285.0 eV).[38] The occurrence of this difference in nonimplanted nNCD$_{Li0}$ films is attributable to the presence of CN species in the growing plasma ($CH_4/H_2/N_2$). CN species have a stronger tendency to bind to the existing diamond clusters,[39,40] forming dangling bonds, which cannot be compensated for effectively by the H$^-$ species. However, this aspect of the study needs a more detailed investigation to confirm such an assumption.

DOI: 10.1021/acsomega.8b01104
ACS Omega 2018, 3, 9956−9965

The C 1s peaks for the $uNCD_{Li14A}$ and $nNCD_{Li14A}$ films were fitted using Lorentzian peaks to evaluate the relative intensities of sp^3 and sp^2 components in these films. In the $uNCD_{Li14A}$ films, the sp^3 fraction is dominant with an intensity of 56.5%, the sp^2 intensity is 43.8% (spectrum I, Figure 6c), whereas the $nNCD_{Li14A}$ films shows an sp^3 peak of 35.4% with an sp^2 peak intensity of 64.6% (spectrum II, Figure 6c). Interestingly, the sp^2 content for the $nNCD_{Li14A}$ films is markedly higher than in the $uNCD_{Li14A}$ films, which is in accordance with the Raman data (cf. Figures 4 and 5). Apparently, a more abundant sp^2 content upon Li-ion implantation and annealing processes in the $nNCD_{Li14A}$ films compared to those in the $uNCD_{Li14A}$ films is also an important factor, resulting in the improvement of the electrical conductivity and FEE properties of the nNCD films (cf. Figures 2 and 3 and Table 1).

Although the variation of the bonding character of NCD films and the surface characteristics of these films owing to Li-ion implantation and annealing processes, which were deduced from micro-Raman spectroscopy and XPS, respectively, is in accordance with the trend for the improvement in the electrical conductivity and the FEE properties of the films, the extent to which the bonding character changes is very small, which makes it unlikely that it can fully account for the large improvement in the electrical conductivity and the FEE properties of NCD. The microstructure of the $uNCD_{Li14A}$ and $nNCD_{Li14A}$ films was investigated using TEM in order to clarify the key factor for enhancing the electrical conductivity and FEE enhancement of the $nNCD_{Li14A}$ films. Figure 7a displays the typical granular structure of the $uNCD_{Li14A}$ films, where only the grains oriented close to some zone-axis strongly diffract electrons and illustrate a high contrast. The nearby grains are oriented away from the zone-axis, presenting no contrast (indicated by an arrow). The distinct spot patterns in the SAED pattern (inset in Figure 7a) designate that the diffraction spots are organized along a ring, representing that the diamond grains were arbitrarily oriented. The high-resolution TEM (HRTEM) micrograph revealed in Figure 7b, which contains the materials in the vicinity of grain boundary, discloses the structure image of region "A" in Figure 7a, demonstrating that the diamond grains comprise a complex microstructure. The Fourier transformed (FT) diffractogram of the whole structure image (FT_0) specifies that the diamond film is basically a cubic diamond structure (3C diamond) oriented in the [011] zone-axis. An FT image of the nominated region "1" (ft_1 image) indicates that the films contain mostly the diamond phase; however, the ft_2 image of the designated region "2" reveals the presence of a-C phases. It should be noted that the diamond grains corresponding to designated region "2" are oriented away from the zone-axis and diffract electrons weakly such that the minor phases situated beneath this grain show up, resulting in a diffuse central ring in the ft_2 image.

Conversely, Figure 8a displays the typical BF-TEM micrograph for the $nNCD_{Li14A}$ films, with the inset displaying a consistent SAED pattern. The SAED contains sharp continuous diffraction rings corresponding to the (111), (220), and (311) lattice planes of the diamond, which indicates the occurrence of randomly oriented small diamond grains. Some regions are of dark contrast, corresponding to diamond grains oriented along a zone-axis that diffracts electrons strongly; however, some regions are of light contrast, corresponding to diamond grains oriented away from the zone-axis that diffracts electrons weakly. A diffuse ring appears in the center of the SAED pattern, signifying the presence of sp^2-bonded carbon (amorphous or crystalline). The HRTEM microstructure image corresponding to region "B" in Figure 8a is revealed in Figure 8b. The FT diffractogram representing the whole structure image is displayed as inset FT_0 of Figure 8b, which entails the diffraction spots organized in ring geometry, representing the occurrence of randomly oriented diamond grains. A weak diffuse ring with donut-geometry is noticeable, suggesting that the sp^2-bonded carbon that exists in these films is nanographite. There are some weak parallel fringes, which are the (111) lattice planes of the diamond, observable all over the structure image in Figure 8b, confirming the presence of diamond in these materials. The diamond and nanographite phases are emphasized by the ft_1 and ft_2 images, being regions "1" and "2" in Figure 8b, correspondingly. Notably, the ft_1 image contains strong diffraction spots, which correspond to the (111) diamond lattice planes (parallel fringes) in region "1", and the central diffuse ring is not observable due to the strong diffraction of electrons by the (111) diamond lattice planes. Only when the diamond grains are oriented away from a zone-axis and diffract electrons weakly can the presence of a central diffuse ring be observed, as shown in the ft_2 image corresponding to region "2". On the basis of the TEM investigations for the $nNCD_{Li14A}$ films, it is concluded that the Li-ion implantation and consecutive annealing process mainly persuade the formation of abundant nanographitic phases.

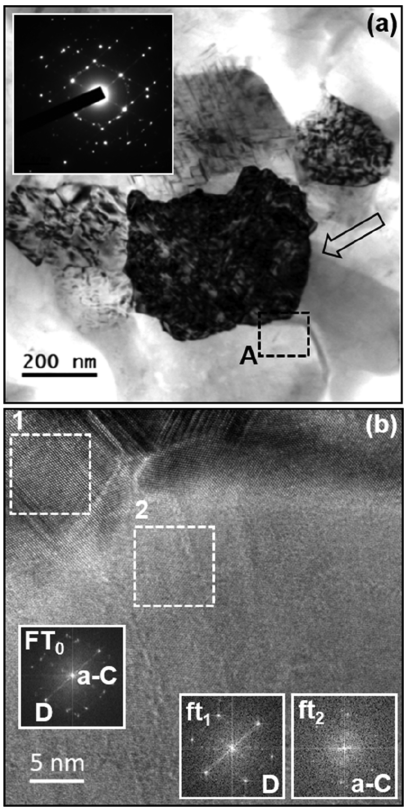

Figure 7. (a) Bright-field TEM micrograph of $uNCD_{Li14A}$ films with the corresponding SAED pattern as inset. (b) HRTEM micrograph, the structure image, of $uNCD_{Li14A}$ films, corresponding to region "A" in "a". Inset FT_0 shows the Fourier-transformed image corresponding to the whole structure image. The ft_1 and ft_2 images show the FT images corresponding to regions "1" and "2" of the structure image, respectively.

DOI: 10.1021/acsomega.8b01104
ACS Omega 2018, 3, 9956−9965

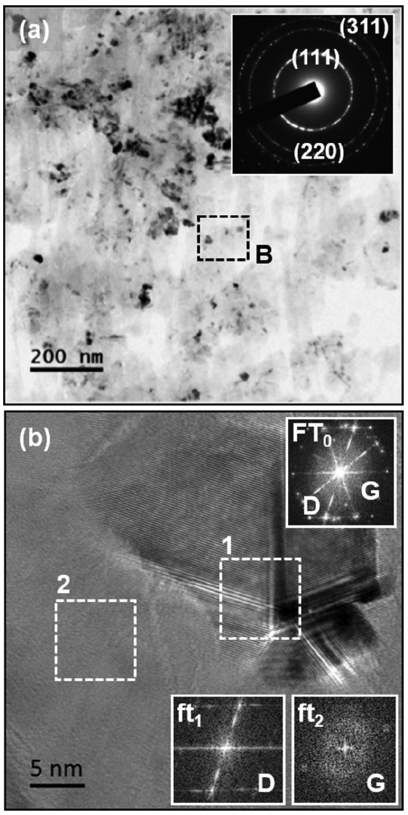

Figure 8. (a) Bright-field TEM micrograph of the $nNCD_{Li14A}$ films with the corresponding SAED pattern as inset. (b) HRTEM micrograph, the structure image, of $nNCD_{Li14A}$ films, corresponding to region "B" in "a". Inset FT_0 shows the Fourier-transformed image corresponding to the whole structure image. The ft_1 and ft_2 images show the FT images corresponding to regions "1" and "2" of the structure image, respectively.

Such an observation is in accordance with the results from Raman and XPS investigations. A similar phase transformation phenomenon might also occur to the $uNCD_{Li14A}$ films but the proportion of the nanographitic phase formed in these films is too small to form an interconnected conduction path. This is, in turn, due to the large grain granular structure of the pristine uNCD films, which comprise very sharp grain boundaries and small proportion of grain boundary phases. The nanographitic phase forms an interconnected network, creating conduction paths for transporting electrons, which is acknowledged as the key factor ensuing greater electrical conductivity and FEE properties for the $nNCD_{Li14A}$ films as compared to those of the $uNCD_{Li14A}$ films.

DISCUSSION

It is stated that a combination of Li-ion implantation and annealing can efficiently increase the electrical conductivity and FEE properties of diamond films. Theoretical studies have proposed that lithium ions can perform as a shallow donor in diamond via occupying the interstitial sites of the materials.[41] Other theoretical calculations visualize a low activation energy for Li diffusion in the crystal lattice of diamond.[17] However, many researchers have tried to dope lithium in diamond via implantation,[42] diffusion (including electro-diffusion),[43,44] adsorption,[45] and accumulation of Li to the gas phase during diamond growth,[46] but none was successful, most likely because Li atoms do not take single interstitial positions but have the tendency to aggregate or couple with other impurities and defects because of their high chemical activity.[47] Moreover, Smith et al.[48] observed that implanted Li ions in polycrystalline diamond films display noticeable diffusion into the grain boundaries of the diamond films when the films were annealed at 1000 °C and above. Accordingly, Li ions tend to reside in grain boundary regions rather than being (interstitially) incorporated into the bulk of the diamond. This implies that Li ions implanted into NCD films tend to reside at the grain boundaries, which can activate the formation of nanographitic phases[20] and, thereby, enhance the FEE properties for these films. Indeed, the abovementioned observations revealed that owing to the existence of abundant grain boundaries in NCD films, the Li-ion implantation/annealing process can efficiently enhance the conductivity and FEE properties of NCD films but not in microcrystalline and single-crystalline diamond films. Similarly, the improvement in electrical conductivity and FEE properties because of the Li-ion implantation/annealing process is better for nNCD films than for uNCD films, which is ascribed to the initiation of more nanographitic phases in nNCD films.

The question that still remains is why the Li-ion implantation/annealing process encourages more abundant sp^2 nanographitic phases in nNCD films than in uNCD films? In order to know this phenomenon, the trajectory of the Li ions in diamond was evaluated using TRIM software. To facilitate the comparison, the same analysis was performed for a-C, which represents the grain boundary phase. The ion range of the Li-implanted ions (50 keV), calculated by TRIM, is 160.3 nm with straggling of 31.0 nm for diamond (Figure 9a) and is 252.4 nm with straggling of 45.5 nm for a-C materials

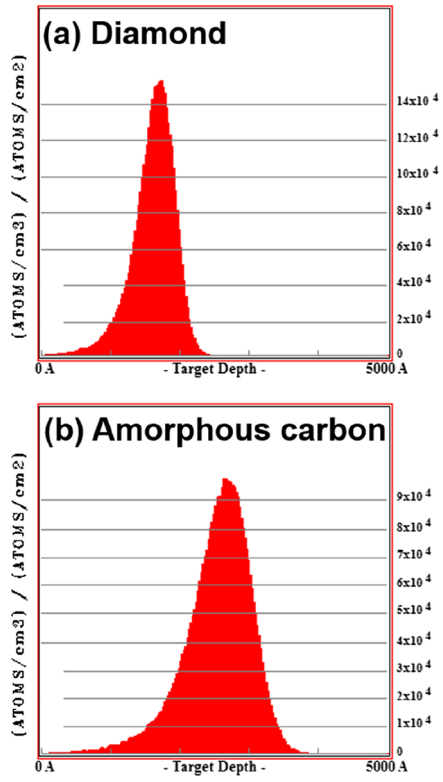

Figure 9. TRIM software calculation to evaluate the trajectory of Li ions (e.g., ion range and straggling) in (a) diamond and (b) a-C materials.

DOI: 10.1021/acsomega.8b01104
ACS Omega 2018, 3, 9956−9965

(Figure 9b). These results indicate that it is much more difficult for Li ions to interact with diamond than with a-C, which explains the unsuccessful incorporation of Li into the bulk of diamond, as observed by Popovici et al.[49]

Time-of-flight secondary ion mass spectroscopy (TOF-SIMS) depth profiles presented in Figure 10 confirm that Li

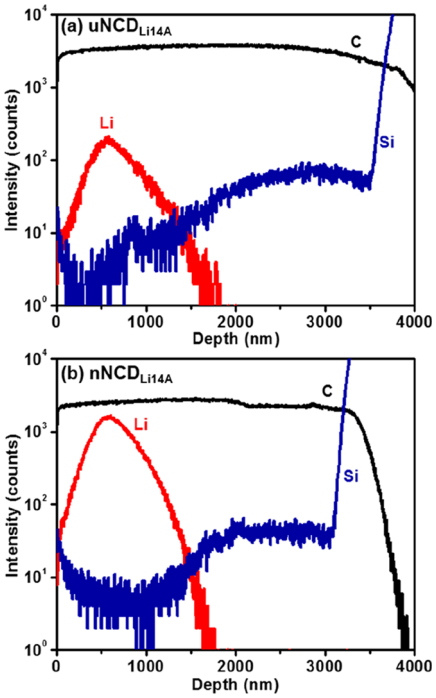

Figure 10. SIMS depth profiles of C, Li, and Si species in (a) uNCD$_{Li14A}$ and (b) nNCD$_{Li14A}$ films.

ions are implanted to a depth of about 1700 nm for the uNCD$_{Li14A}$ and nNCD$_{Li14A}$ films. However, the peak concentration is located at around 575 nm beneath the surface for the nNCD$_{Li14A}$ films (Figure 10b), which is slightly higher than the peak concentration of the uNCD$_{Li14A}$ films (~560 nm; Figure 10a). As mentioned earlier, the uNCD films comprise faceted diamond grains with sharp grain boundaries, whereas the nNCD films possess wider grain boundaries, which contain *t*-PA phases. The implanted Li ions can capably interrelate with the *t*-PA phases in the grain boundaries of nNCD films, dissociating the *t*-PA phase into disordered carbon (or a-C), which is in accordance with the TRIM calculation (Figure 9). The implanted Li ions can also desorb H and induce the formation of dangling bonds, which act as electron trap centers. Annealing at 1000 °C effectively healed the atomic defects induced in the diamond grains (electron trap centers were eliminated) and converted the disordered carbon (or a-C) in the grain boundaries into the nanographitic phase. The phase transformation of disordered carbon (or a-C) into nanographitic phases was facilitated by the catalytic effect of the Li ions existing in the grain boundaries.[20] All these processes improved the electrical conductivity and FEE characteristics of the nNCD$_{Li14A}$ films.[6,12,13] Consequently, the implanted Li ions are much more efficient in inducing the formation of nanographitic phases in the grain boundaries of the nNCD films compared to the uNCD films and enhance the electrical conductivity and FEE properties for these films. The difference in electrical conductivity and FEE behavior of Li-ion-implanted and annealed nNCD and uNCD films is caused by the difference in granular structure as well as the bonding characteristics of the two pristine nNCD and uNCD films.

CONCLUSIONS

The characteristics of NCD films were methodically examined to understand the roles of lithium-ion implantation and annealing in enhancing the electrical and FEE properties of NCD films. Micro-Raman and XPS studies indicated that Li-ion implantation encouraged electron trap centers in both uNCD and nNCD films. Postannealing restored the atomic defects and transformed the disordered carbon (or a-C phase) into more stable nanographitic phases. The more abundant nanographitic phases were present in the grain boundaries of the nNCD$_{Li14A}$ films that organized an interrelated path for electron transport and improved more markedly the electrical conductivity and FEE properties of the nNCD$_{Li14A}$ films associated with other kinds of NCD films, especially the uNCD films. The superior electrical conductivity and FEE characteristics of the nNCD$_{Li14A}$ films via Li-ion implantation and postannealing processes open the prospect of using such material for device applications.

EXPERIMENTAL METHODS

The Si(100) substrates were seeded by a water-based state-of-the-art colloidal suspension of 5 nm detonation nanodiamonds.[50] For synthesizing the NCD films, the seeded Si substrates were then placed in an ASTeX 6500 series microwave plasma-enhanced chemical vapor deposition reactor. A gas mixture of CH_4 (3 sccm) and H_2 (297 sccm) (CH_4/H_2 = 1/99) was used for the growth of uNCD films and a gas mixture of CH_4 (18 sccm), H_2 (267), and N_2 (15 sccm) ($CH_4/H_2/N_2$ = 6/89/5) was used as the starting gas mixture for the growth of nNCD films. The microwave power of 3000 W and the total pressure of 30 Torr were maintained for the preparation of both pristine NCD films. The substrate temperature was measured using an optical pyrometer and was estimated to be around 675 °C during the growth of the uNCD films and around 540 °C during the growth of the nNCD films. Both NCD films were grown to a thickness of 500 nm. Lithium ion implantations were then executed on both these NCD films with an implantation energy of 50 keV (EATON, 200 kV) using ion doses of 10^{12} to 10^{14} ions/cm^2 at room temperature. The ion-implanted NCD films were further annealed at 1000 °C for 30 min under vacuum (3×10^{-5} Torr; typical base pressure: 2×10^{-6} Torr).

SEM (FEI Quanta 200 FEG microscope), TEM (JEOL 2100F), confocal micro-Raman spectroscopy (a Horiba Jobin-Yvon T64000 spectrometer; λ = 488 nm and spot size = ~1 μm), and TOF-SIMS (an ION-TOF 5 system (IONTOF GmbH) were performed; the analyzer was operated in the positive polarity mode with a Bi3+ ion source (30 kV) for analysis and an O_2^+ ion source (2 kV) for sputtering; depth profiling was performed in the spectrometry mode(non-interlaced) with a reflector voltage of 200 V, a cycle time of 200 μs, a sampling area of 100 × 100 μm^2, and sputtering area of 300 × 300 μm^2; charge compensation was performed using a flood gun. The TOF-SIMS spectra were mass-calibrated on the C_xH_y fragments and XPS (Thermo-VG Scientific ESCALab 250 Microprobe equipped with a monochromatic Al Kα X-ray source (1486.6 eV); pressure = 10^{-9} Torr) was used to characterize the diamond samples. Hall measurements in a van der Pauw configuration (ECOPIA HMS-3000) were used to

DOI: 10.1021/acsomega.8b01104
ACS Omega 2018, 3, 9956−9965

estimate the electrical conductivity of these films. The FEE properties of the NCD films were measured with a tunable parallel cathode−anode setup, in which the anode was a molybdenum rod of 2 mm diameter and the sample-to-anode distance was controlled using a micrometer. The current−voltage (I−V) characteristics were measured using an electrometer (Keithley 2410) at a pressure below 10^{-6} Torr.[12]

AUTHOR INFORMATION

Corresponding Authors

*E-mail: sankaran.kamatchi@uhasselt.be (K.J.S.).
*E-mail: inanlin@mail.tku.edu.tw (I.-N.L.).
*E-mail: ken.haenen@uhasselt.be (K.H.).

ORCID

Kamatchi Jothiramalingam Sankaran: 0000-0002-4468-0541
Sien Drijkoningen: 0000-0003-1807-0018
Kam Tong Leung: 0000-0002-1879-2806
I-Nan Lin: 0000-0001-6474-2394
Ken Haenen: 0000-0001-6711-7367

Notes

The authors declare no competing financial interest.

ACKNOWLEDGMENTS

The authors would like to thank the financial support of the Research Foundation Flanders (FWO) via Research Grants 12I8416N and 1519817N, and the Methusalem "NANO" network. K.J.S. and P.P. are Postdoctoral Fellows of the Research Foundation Flanders (FWO). The Hercules Foundation Flanders is acknowledged for financial support of the Raman equipment.

REFERENCES

(1) Lin, S.-C.; Yeh, C.-J.; Manoharan, D.; Leou, K.-C.; Lin, I.-N. Microstructural Evolution of Nanocrystalline Diamond Films Due to CH4/Ar/H2 Plasma Post-Treatment Process. *ACS Appl. Mater. Interfaces* **2015**, *7*, 21844−21851.

(2) Ficek, M.; Sankaran, K. J.; Ryl, J.; Bogdanowicz, R.; Lin, I.-N.; Haenen, K.; Darowicki, K. Ellipsometric investigation of nitrogen doped diamond thin films grown in microwave CH4/H2/N2 plasma enhanced chemical vapor deposition. *Appl. Phys. Lett.* **2016**, *108*, 241906.

(3) Sankaran, K. J.; Kumar, N.; Kurian, J.; Ramadoss, R.; Chen, H.-C.; Dash, S.; Tyagi, A. K.; Lee, C.-Y.; Tai, N.-H.; Lin, I.-N. Improvement in Tribological Properties by Modification of Grain Boundary and Microstructure of Ultrananocrystalline Diamond Films. *ACS Appl. Mater. Interfaces* **2013**, *5*, 3614−3624.

(4) Stehlik, S.; Varga, M.; Stenclova, P.; Ondic, L.; Ledinsky, M.; Pangrac, J.; Vanek, O.; Lipov, J.; Kromka, A.; Rezek, B. Ultrathin Nanocrystalline Diamond Films with Silicon Vacancy Color Centers via Seeding by 2 nm Detonation Nanodiamonds. *ACS Appl. Mater. Interfaces* **2017**, *9*, 38842−38853.

(5) Williams, O. A.; Nesládek, M. Growth and Properties of Nanocrystalline Diamond Films. *Phys. Status Solidi A* **2006**, *203*, 3375−3386.

(6) Ikeda, T.; Teii, K. Origin of Low Threshold Field Emission from Nitrogen-Incorporated Nanocrystalline Diamond Films. *Appl. Phys. Lett.* **2009**, *94*, 143102.

(7) Sankaran, K. J.; Kalpataru, P.; Balakrishnan, S.; Tai, N.-H.; Lin, I.-N. Catalytically Induced Nanographitic Phase by a Platinum-ion Implantation/annealing Process to Improve the Field Electron Emission Properties of Ultrananocrystalline Diamond Films. *J. Mater. Chem. C* **2015**, *3*, 2632−2641.

(8) Panda, K.; Hyeok, J. J.; Park, J. Y.; Sankaran, K. J.; Balakrishnan, S.; Lin, I. N. Nanoscale Investigation of Enhanced Electron Field Emission for Silver Ion Implanted/Postannealed Ultrananocrystalline Diamond Films. *Sci. Rep.* **2017**, *7*, 16325.

(9) Arenal, R.; Bruno, P.; Miller, D. J.; Bleuel, M.; Lal, J.; Gruen, D. M. Diamond Nanowires and the Insulator-Metal Transition in Ultrananocrystalline Diamond Films. *Phys. Rev. B: Condens. Matter Mater. Phys.* **2007**, *75*, 195431.

(10) Talapatra, S.; Cheng, J.-Y.; Chakrapani, N.; Trasobares, S.; Cao, A.; Vajtai, R.; Huang, M. B.; Ajayan, P. M. Ion Irradiation Induced Structural Modifications in Diamond Nanoparticles. *Nanotechnology* **2006**, *17*, 305−309.

(11) Hu, X. J.; Ye, J. S.; Hu, H.; Chen, X. H.; Shen, Y. G. Phosphorus Ion Implantation and Annealing Induced n-type Conductivity and Microstructure Evolution in Ultrananocrystalline Diamond Films. *Appl. Phys. Lett.* **2011**, *99*, 131902.

(12) Sankaran, K. J.; Chen, H.-C.; Panda, K.; Sundaravel, B.; Lee, C.-Y.; Tai, N.-H.; Lin, I.-N. Enhanced Electron Field Emission Properties of Conducting Ultrananocrystalline Diamond Films after Cu and Au Ion Implantation. *ACS Appl. Mater. Interfaces* **2014**, *6*, 4911−4919.

(13) Panda, K.; Inami, E.; Sugimoto, Y.; Sankaran, K. J.; Lin, I.-N. Straight Imaging and Mechanism Behind Grain Boundary Electron Emission in Pt-doped Ultrananocrystalline Diamond Films. *Carbon* **2017**, *111*, 8−17.

(14) Lin, S.-C.; Yeh, C.-J.; Dong, C. L.; Niu, H.; Kurian, J.; Leou, K.-C.; Lin, I.-N. The Microstructural Evolution of Ultrananocrystalline Diamond Films Due to P Ion Implantation and Annealing Process-Dosage Effect. *Diamond Relat. Mater.* **2015**, *54*, 47−54.

(15) Palathinkal, T. J.; Tai, N.-H.; Lee, C.-Y.; Niu, H.; Cheng, H.-F.; Pong, W.-F.; Lin, I.-N. Field Emission Enhancement in Ion Implanted Ultra-nanocrystalline Diamond Films. *Plasma Processes Polym.* **2009**, *6*, S834−S839.

(16) Hu, X. J.; Ye, J. S.; Liu, H. J.; Shen, Y. G.; Chen, X. H.; Hu, H. n-type Conductivity and Phase Transition in Ultrananocrystalline Diamond Films by Oxygen Ion Implantation and Annealing. *J. Appl. Phys.* **2011**, *109*, 053524.

(17) Bernholc, J.; Kajihara, S. A.; Wang, C.; Antonelli, A.; Davis, R. F. Theory of Native Defects, Doping and Diffusion in Diamond and Silicon Carbide. *Mater. Sci. Eng., B* **1992**, *11*, 265−272.

(18) Job, R.; Werner, M.; Denisenko, A.; Zaitsev, A.; Fahrner, W. R. Electrical Properties of Lithium-Implanted Layers on Synthetic Diamond. *Diamond Relat. Mater.* **1996**, *5*, 757−760.

(19) Vavilov, V. S.; Gukasyan, M. A.; Guseva, M. I.; Konorova, E. A. Electrical Conductivity of Diamond Containing. Implanted Lithium Ions. *Sov. Phys. Semicond.* **1972**, *6*, 741−746.

(20) Sankaran, K. J.; Srinivasu, K.; Yeh, C. J.; Thomas, J. P.; Drijkoningen, S.; Pobedinskas, P.; Sundaravel, B.; Leou, K. C.; Leung, K. T.; Van Bael, M. K.; Schreck, M.; Lin, I. N.; Haenen, K. Field electron emission enhancement in lithium implanted and annealed nitrogen-incorporated nanocrystalline diamond films. *Appl. Phys. Lett.* **2017**, *110*, 261602.

(21) Teng, K.-Y.; Chen, H.-C.; Tang, C.-Y.; Sundaravel, B.; Amirthapandian, S.; Lin, I.-N. Microstructure Evolution and The Modification of the Electron Field Emission Properties of Diamond Films by Gigaelectron Volt Au-Ion Irradiation. *AIP Adv.* **2011**, *1*, 042108.

(22) Mortet, V.; Zhang, L.; Eckert, M.; D'Haen, J.; Soltani, A.; Moreau, M.; Troadec, D.; Neyts, E.; De Jaeger, J.-C.; Verbeeck, J.; Bogaerts, A.; Van Tendeloo, G.; Haenen, K.; Wagner, P. Grain Size Tuning of Nanocrystalline Chemical Vapor Deposited Diamond by Continuous Electrical Bias Growth: Experimental and Theoretical Study. *Phys. Status Solidi A* **2012**, *209*, 1675−1682.

(23) Ferrari, A. C.; Robertson, J. Origin of the 1150 cm^{-1} Raman Mode in Nanocrystalline Diamond. *Phys. Rev. B: Condens. Matter Mater. Phys.* **2001**, *63*, 121405−121409.

(24) Michler, J.; von Kaenel, Y.; Stiegler, J.; Blank, E. Complementary Application of Electron Microscopy and micro-Raman Spectroscopy for Microstructure, Stress, and Bonding Defect Investigation of Heteroepitaxial Chemical Vapor Deposited Diamond Films. *J. Appl. Phys.* **1998**, *83*, 187−197.

DOI: 10.1021/acsomega.8b01104
ACS Omega 2018, 3, 9956−9965

(25) Ferrari, A. C.; Robertson, J. Interpretation of Raman Spectra of Disordered and Amorphous Carbon. *Phys. Rev. B: Condens. Matter Mater. Phys.* **2000**, *61*, 14095−14107.
(26) Ilie, A.; Ferrari, A. C.; Yagi, T.; Rodil, S. E.; Robertson, J.; Barborini, E.; Milani, P. Role of sp2 Phase in Field Emission from Nanostructured Carbons. *J. Appl. Phys.* **2001**, *90*, 2024−2032.
(27) Fowler, R. H.; Nordheim, L. Electron Emission in Intense Electric Fields. *Proc. R. Soc. London, Ser. A* **1928**, *119*, 173−181.
(28) Mapelli, C.; Castiglioni, C.; Zerbi, G.; Müllen, K. Common Force Field for Graphite and Polycyclic Aromatic Hydrocarbons. *Phys. Rev. B: Condens. Matter Mater. Phys.* **1999**, *60*, 12710−12725.
(29) Lee, S. T.; Peng, H. Y.; Zhou, X. T.; Wang, N.; Lee, C. S.; Bello, I.; Lifshitz, Y. A Nucleation Site and Mechanism Leading to Epitaxial Growth of Diamond Films. *Science* **2000**, *287*, 104−106.
(30) Ferrari, A. C.; Robertson, J. Resonant Raman Spectroscopy of Disordered, Amorphous, and Diamondlike Carbon. *Phys. Rev. B: Condens. Matter Mater. Phys.* **2001**, *64*, 075414.
(31) Zhu, W.; Kochanski, G. P.; Jin, S.; Seibles, L. Defect-enhanced electron field emission from chemical vapor deposited diamond. *J. Appl. Phys.* **1995**, *78*, 2707−2711.
(32) Zhu, W.; Kochanski, G. P.; Jin, S.; Seibles, L.; Jacobson, D. C.; McCormack, M.; White, A. E. Electron field emission from ion-implanted diamond. *Appl. Phys. Lett.* **1995**, *67*, 1157−1159.
(33) Panda, K.; Sankaran, K. J.; Panigrahi, B. K.; Tai, N.-H.; Lin, I.-N. Direct Observation and Mechanism for Enhanced Electron Emission in Hydrogen Plasma-Treated Diamond Nanowire Films. *ACS Appl. Mater. Interfaces* **2014**, *6*, 8531−8541.
(34) Fan, Y.; Fitzgerald, A. G.; John, P.; Troupe, C. E.; Wilson, J. I. B. X-ray Photoelectron Spectroscopy Studies of CVD Diamond Films. *Surf. Interface Anal.* **2002**, *34*, 703−707.
(35) Hoffman, A.; Andrienko, I.; Jamieson, D. N.; Prawer, S. Electron Trapping and Detrapping in Ion-Beam-Damaged Diamond Surfaces. *Appl. Phys. Lett.* **2005**, *86*, 044103.
(36) Zhou, D.; McCauley, T. G.; Qin, L. C.; Krauss, A. R.; Gruen, D. M. Synthesis of Nanocrystalline Diamond Thin Films from an Ar-CH4 Microwave Plasma. *J. Appl. Phys.* **1998**, *83*, 540−543.
(37) Joseph, P. T.; Tai, N. H.; Lee, C.-Y.; Niu, H.; Pong, W. F.; Lin, I. N. Field Emission Enhancement in Nitrogen-Ion-Implanted Ultrananocrystalline Diamond Films. *J. Appl. Phys.* **2008**, *103*, 043720.
(38) Talapatra, S.; Ganesan, P. G.; Kim, T.; Vajtai, R.; Huang, M.; Shima, M.; Ramanath, G.; Srivastava, D.; Deevi, S. C.; Ajayan, P. M. Irradiation-induced Magnetism in Carbon nanostructures. *Phys. Rev. Lett.* **2005**, *95*, 097201.
(39) Saravanan, A.; Huang, B.-R.; Sankaran, K. J.; Tai, N.-H.; Lin, I.-N. Highly Conductive Diamond-Graphite Nanohybrid Films with Enhanced Electron Field Emission and Microplasma Illumination Properties. *ACS Appl. Mater. Interfaces* **2015**, *7*, 14035−14042.
(40) Lin, C.-R.; Liao, W.-H.; Wei, D.-H.; Tsai, J.-S.; Chang, C.-K.; Fang, W.-C. Formation of Ultrananocrystalline Diamond Films with Nitrogen Addition. *Diamond Relat. Mater.* **2011**, *20*, 380−384.
(41) Goss, J. P.; Eyre, R. J.; Briddon, P. R. Theoretical Models For Doping Diamond For Semiconductor Applications. *Phys. Status Solidi B* **2008**, *245*, 1679−1700.
(42) Khmelnitsky, R. A.; Saraykin, V. V.; Dravin, V. A.; Zavedeyev, E. V.; Makarov, S. V.; Bronsky, V. S.; Gippius, A. A. Lithium Implanted into Diamond: Regular Trends and Anomalies. *Surf. Coat. Technol.* **2016**, *307*, 236−242.
(43) te Nijenhuis, J.; Cao, G. Z.; Smits, P. C. H. J.; van Enckevort, W. J. P.; Giling, L. J.; Alkemade, P. F. A.; Nesládek, M.; Remeš, Z. Incorporation of Lithium in Single Crystal Diamond: Diffusion Profiles and Optical and Electrical Properties. *Diamond Relat. Mater.* **1997**, *6*, 1726−1732.
(44) Uzan-Saguy, C.; Cytermann, C.; Fizgeer, B.; Richter, V.; Brener, R.; Kalish, R. Diffusion of Lithium in Diamond. *Phys. Status Solidi A* **2002**, *193*, 508−516.
(45) O'Donnell, K. M.; Martin, T. L.; Edmonds, M. T.; Tadich, A.; Thomsen, L.; Ristein, J.; Pakes, C. I.; Fox, N. A.; Ley, L. Photoelectron Emission from Lithiated Diamond. *Phys. Status Solidi A* **2014**, *211*, 2209−2222.
(46) Zamir Othman, M.; May, P. W.; Fox, N. A.; Heard, P. J. Incorporation of Lithium and Nitrogen into CVD Diamond Thin Films. *Diamond Relat. Mater.* **2014**, *44*, 1−7.
(47) Popovici, G.; Sung, T.; Khasawinah, S.; Prelas, M. A.; Wilson, R. G. Forced Diffusion of Impurities in Natural Diamond and Polycrystalline Diamond Films. *J. Appl. Phys.* **1995**, *77*, 5625−5629.
(48) Smith, S. P.; Landstrass, M. I.; Wilson, R. G. In *Secondary Ion Mass Spectrometry, SIMS VIII*; Benninghoven, A., Janssen, K. T. F., Tumpner, J., Werner, H. W., Eds.; Wiley: New York, 1992; pp 159−170.
(49) Popovici, G.; Wilson, R. G.; Sung, T.; Prelas, M. A.; Khasawinah, S. Diffusion of Boron, Lithium, Oxygen, Hydrogen, and Nitrogen in Type IIa Natural Diamond. *J. Appl. Phys.* **1995**, *77*, 5103−5106.
(50) Williams, O. A.; Douhéret, O.; Daenen, M.; Haenen, K.; Ōsawa, E.; Takahashi, M. Enhanced Diamond Nucleation on Monodispersed Nanocrystalline Diamond. *Chem. Phys. Lett.* **2007**, *445*, 255−258.

DOI: 10.1021/acsomega.8b01104
ACS Omega 2018, 3, 9956−9965